

A study of 3-dimensional shapes of asteroid families with an application to Eos

M. Brož

Institute of Astronomy, Charles University, Prague, V Holešovičkách 2, 18000 Prague 8, Czech Republic e-mail: mira@sirrah.troja.mff.cuni.cz

A. Morbidelli

Observatoire de la Côte d'Azur, BP 4229, 06304 Nice Cedex 4, France, e-mail: morby@oca.eu

Abstract

In order to fully understand **the** shapes of asteroids families in the 3-dimensional space of the proper elements ($a_p, e_p, \sin I_p$) it is necessary to compare observed asteroids with N-body simulations. To this point, we describe a rigorous yet simple method which allows for a selection of the observed asteroids, assures the same size-frequency distribution of synthetic asteroids, accounts for a background population, and computes a χ^2 metric. We study **the** Eos family as an example, and we are able to fully explain its non-isotropic features, including the distribution of pole latitudes β . We confirm its age $t = (1.3 \pm 0.3)$ Gyr; while this value still scales with the bulk density, it is verified by a Monte-Carlo collisional model. The method can be applied to other populous families (Flora, Eunomia, Hygiea, Koronis, Themis, **Vesta**, etc.).

1. Introduction

A rigorous comparison of observations *versus* simulations of asteroid families is a rather difficult task, especially when the observations look like Figure 1. Observed proper elements $a_p, e_p, \sin I_p$, supplied by physical data (colour indices $a^*, i - z$ in this case), show a complicated structure of **the** Eos family halo, together with many neighbouring families, overlapping halos, and background asteroids, of course. The hierarchical clustering method alone (HCM, Zappalà et al. 1995) is then practically useless.

Family identification itself affects dynamical studies and *vice versa*. We would need the family to determine initial conditions. On the other hand, we would need a dynamical study to understand wherever family members could be. There are several well-known weaknesses of HCM, which were demonstrated e.g. in a ‘crime-scene’ Fig. 8 of Nesvorný et al. (2015). The HCM needs a free parameter, either the cutoff velocity v_{cut} , or the quasi-random level QRL. It is also unable to associate halos. Last but not least, the background is never precisely uniform what can be clearly seen at the edges of currently stable zones, close or inside gravitational resonances, or even in stable zones where the population was deteriorated by dynamical processes in the distant past (cf. Cybele region; Carruba et al. 2015).

On the other hand, synthetic families evolve in the course of simulation and lose their members, consequently we should use a variable v_{cut} , but its optimal value is again generally unknown. No direct comparison is thus possible.

That is a motivation for our work. We describe a method suitable to study 3-dimensional shapes of asteroid families, taking into account all proper orbital elements, including possibly non-uniform background, and matching the size-frequency dis-

tribution at the same time. Our method still relies on a preliminary selection of observed asteroids according to their colours (or albedos) to suppress – but *not* fully exclude – interlopers. A comparison of the observed asteroids with an output of N-body simulation is performed by means of counting the bodies in proper-element ‘boxes’, and a suitable χ^2 metric. Because we are forced to select synthetic asteroids randomly (a Monte-Carlo approach), we can expect some stochasticity of the results.

We present an application to **the** Eos family (family identification number, FIN = 606), one of the most studied families to date, mentioned already by Hirayama (1918). Together with our previous works (Vokrouhlický et al., 2006; Brož and Morbidelli, 2013), this paper forms a long-term series focused on its long-term evolution. We use up-to-date catalogues of proper elements (Knežević and Milani, 2003), and brand new spin data (Hanuš et al., 2018).

Let us recall **that the** Eos family is of K taxonomic type, while the background is mostly C type. Mothé-Diniz et al. (2008) suggested either a partially differentiated parent body, with meteorite analogues CV, CO or R; or a undifferentiated one, with CK analogues. There was a discovery of a recent breakup of (6733) 1992 EF (Novaković and Tsirvoulis, 2014), belonging to the family core, what makes Eos even more interesting for space weathering studies, because we may see both old (1.3 Gyr) and young (4 Myr) surfaces.

2. Methods

Before we proceed with the description of the method, let us explain three problems we have to solve and describe the underlying dynamical model.

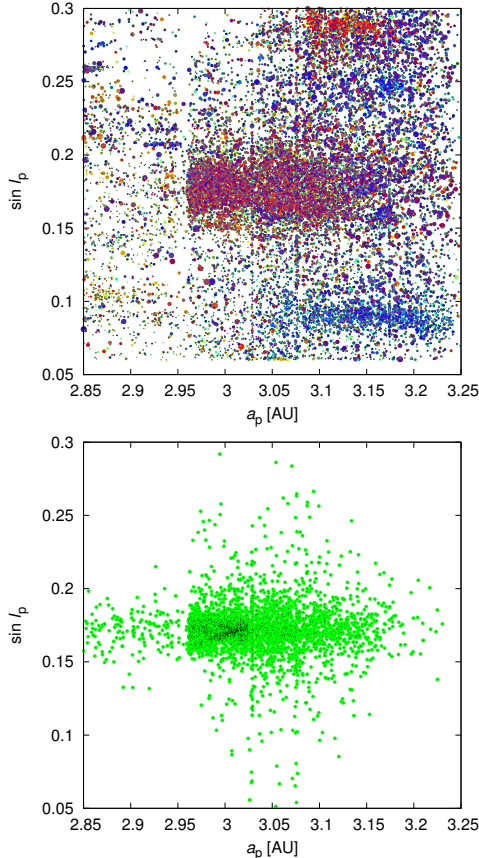


Figure 1: Top panel: the proper semimajor axis a_p vs proper inclination $\sin I_p$ for all asteroids in the broad surroundings of Eos family. The range of proper eccentricities is $e_p \in (0.0; 0.3)$. If they have colour data in the SDSS MOC4 catalogue (Parker et al., 2008), the colours correspond to indices a^* , $i-z$ which are closely related to taxonomy, namely blue is close to C-complex taxonomy, red to S-complex, and magenta to K-type. The whole sample contains 18471 asteroids. There are other prominent families visible: Hygeia (C-type, bottom-right), Veritas (C, next to Eos), Tirela (S, upper right), Telramund (S, below Eos); a close inspection would show 32 families in total! Bottom panel: the same plot for a typical outcome of N-body simulations, assuming a disruption of a parent body, ejection of fragments with some velocity field, and their long-term dynamical evolution due to gravitational perturbations, resonances, chaotic diffusion, the Yarkovsky effect, the YORP effect, etc. The two panels are not directly comparable.

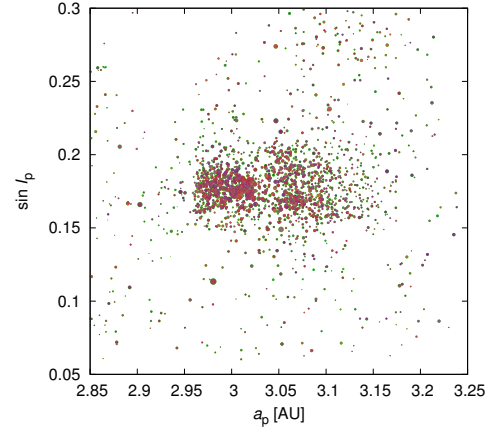


Figure 2: K-type asteroids selected from Figure 1, with known colour indices $a^* \in (0.0; 0.1)$, $i-z \in (-0.03; 0.08)$. The visual geometric albedo had to be $p_V > 0.07$ (or unknown). This subset is much more homogeneous and contains 1991 asteroids. No other prominent families except Eos can be seen; the only exception may be some contamination by Tirela (upper right) due to inherent photometric noise. This subset seems already suitable for a comparison with N-body simulations.

2.1. Problem 1: Selection of asteroids

In principle, we can select any subset of asteroids (e.g. by using SDSS colour data, or WISE albedo data) to decrease a contamination by interlopers, or an overlap with other families in the neighbourhood (Parker et al., 2008; Masiero et al., 2011); **an approach also used in a multidomain HCM (Carruba et al., 2013)**. We can also simulate any subset at will, but we should definitely check surroundings where the bodies can be scattered to, because this may be a key constraint.

For Eos family, it is easy because of its distinct K taxonomic type which is defined for our purposes in terms of the SDSS colour indices $a^* \in (0.0, 0.1)$, $i-z \in (-0.03, 0.08)$, and the geometric albedo $p_V > 0.07$ (if known **in WISE or IRAS catalogues**). If only colours are known, we select the asteroids according to them, and assume their $p_V = 0.158$ which corresponds to the median value of Eos members. As a result, only 1/10th of asteroids remain, but this is still sufficient (Figure 2). Practically all **other** families have disappeared, the background is much more uniform. The only exception may be some contamination from **the** Tirela family (seen as a concentration in the upper right corner of Fig. 2), arising from a photometric noise on S-type asteroids, and a gap at large $\sin I_p > 0.25$.

Regarding the homogeneity of albedos, the WISE data exhibit a wide distribution. The uncertainties σ_p arise mainly from photon noise, and NEATM model systematics. In a statistical sense, even the single albedo value $\bar{p}_V = 0.158$ would result in a relatively wide distribution because σ_p values are relatively large, which is demonstrated in Figure 3.

2.2. Problem 2: Size-frequency distribution

The size-frequency distributions (SFDs) should match for both the observed and synthetic populations, but the latter changes in the course of time (Figure 4). In order to compare apples with apples, we have to scale the SFD. In other words,

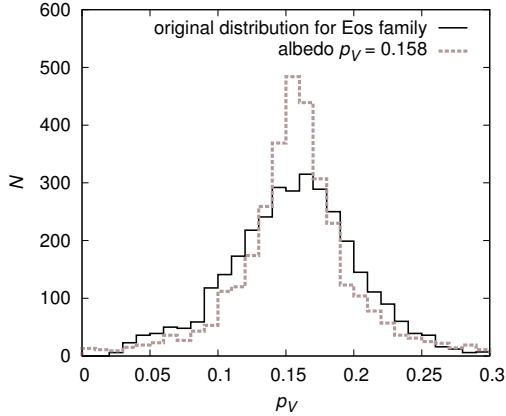


Figure 3: The observed differential distribution of visual geometric albedos p_V for the Eos family from the WISE catalogue (Masiero et al., 2011) (black solid), and for the same set of bodies with p_V values assigned randomly, assuming a Gaussian distribution with a constant mean $\bar{p}_V = 0.158$, and $1\text{-}\sigma$ uncertainty declared in the catalogue (dashed gray). The widths of the two distributions are similar, so using the constant \bar{p}_V (if unknown) is *not* a poor approximation.

96 we randomly select the same number of synthetic bodies (to-
 97 gether with their orbits, of course) as the number of observed
 98 bodies, in each of prescribed size bins ($D, D + dD$). To this
 99 point, it is definitively useful to start with a larger number of
 100 synthetic bodies, so that we still have more than observed at the
 101 end of simulation.

102 This random selection of synthetic asteroids to match the
 103 SFD of observed asteroids is needed at every single **output**
 104 time step of the simulation. Even multiple selections at one time
 105 step might be useful. This way, we would naturally account for an
 106 additional (and often neglected) uncertainty which arises from
 107 the fact we always choose the initial conditions from some un-
 108 derlying distributions (e.g. from a prescribed velocity field), but
 109 we cannot be absolutely sure that our single selection is not a
 110 lucky fluke.

111 2.3. Problem 3: Non-uniform background

112 A background has to be accounted for otherwise it is essen-
 113 tially impossible to explain a lot of bodies far from the family.
 114 First, we need to find some observed background, not very far
 115 from the family; in our case, a suitable population seems to be
 116 at $\sin I_p \in (0.06; 0.12)$ and $(0.24; 0.30)$. It has its own size-
 117 frequency distribution, and we should use the same SFD for the
 118 synthetic background. As a first approximation, we model the
 119 background as a random uniform distribution in the space of
 120 proper elements.

121 However, Murphy’s law for backgrounds states: **The back-**
 122 **ground is never uniform.** Especially below and above the 7/3
 123 mean-motion resonance with Jupiter we can expect a difference
 124 (see the example in Figure 5).

125 Again, there is a non-negligible stochasticity. We shall at
 126 least try a different random seed. The number density of back-
 127 ground objects can be also treated as a free parameter. There is
 128 also *a priori* unknown systematic contamination by neighbour-
 129 ing families, but this is not necessarily present right ‘under’ the
 130 Eos family.

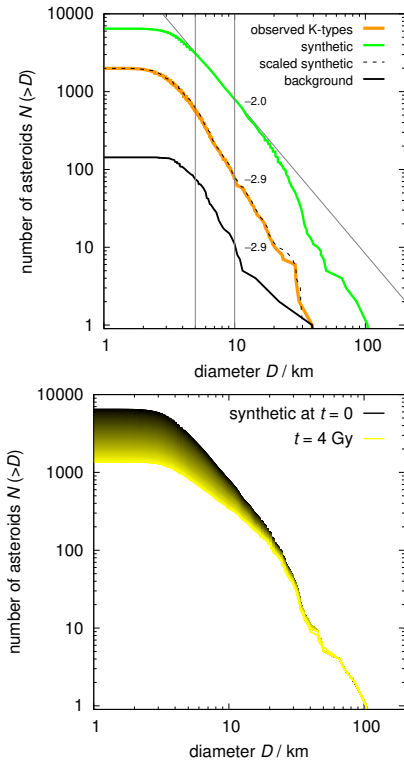


Figure 4: Top panel: the cumulative size-frequency distribution (SFD) of the observed K-type asteroids (orange), the synthetic SFD at the beginning of N-body simulation (green), the *scaled* synthetic SFD constructed by a random selection of bodies so that it matches the observed one (dotted black; hard to distinguish from orange), and the background SFD (black). Bottom panel: an evolution of the synthetic SFD in the course of an N-body simulation, from time $t = 0$ up to 4 Gyr, which is indicated by changing colours (black \rightarrow yellow). These changes (due to a dynamical decay) require scaling at every time step.

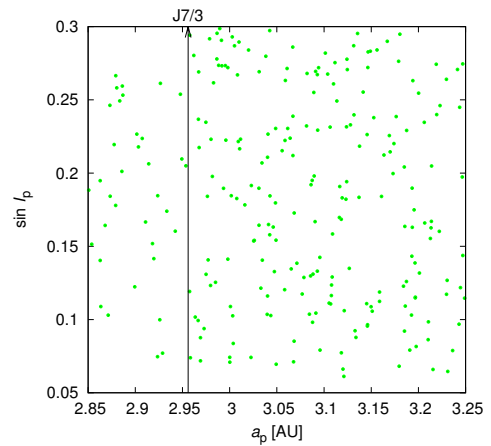


Figure 5: A synthetic background generated as a random uniform distribution in proper orbital elements $a_p, e_p, \sin I_p$, with the same size-distribution as the observed background. In this example, the number densities below and above the 7/3 mean-motion resonance with Jupiter at 2.956 au are different (by a factor of 2), because this resonance separates two distinct zones of the main belt.

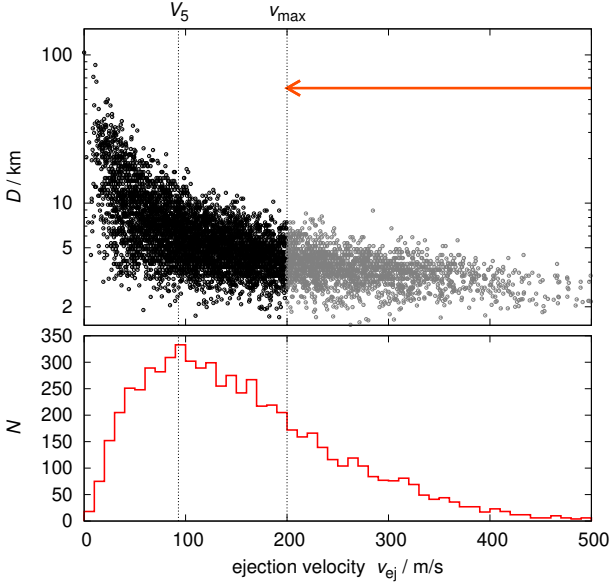


Figure 6: Top panel: the dependence of the ejection velocity v_{ej} on the diameter D for our synthetic bodies. The value $V_5 = 93 \text{ m s}^{-1}$ denotes the dispersion of velocity components for $D_5 = 5 \text{ km}$ bodies. In specific cases (Sec. 3.2), we select only bodies with velocities smaller than some maximum value, $v_{ej} < v_{max}$. Bottom panel: the corresponding histogram of v_{ej} .

2.4. Dynamical model

Our dynamical model was described in detail in Brož et al. (2011). We briefly recall it contains a modified SWIFT integrator (Levison and Duncan, 1994; Laskar and Robutel, 2001), both the diurnal and seasonal Yarkovsky thermal effects (Vokrouhlický, 1998; Vokrouhlický and Farinella, 1999), which induce a semimajor axis drift da/dt ; all mean-motion and secular resonances, captures and corresponding drifts de/dt , dI/dt , the YORP effect, changing the spin rate ω and the obliquity γ (Čapek and Vokrouhlický, 2004), with the efficiency parameter $c_{YORP} = 0.33$ (Hanuš et al., 2011), simplified collisional reorientations by means of a prescribed time scale dependent on size D (Farinella et al., 1998), random period changes due to mass shedding after reaching the critical spin rate ω_{crit} (Pravec and Harris, 2000), and suitable digital filters for computations of mean and proper elements (Quinn et al., 1991; Šidlichovský and Nesvorný, 1996).

Initial conditions are kept as simple as possible. We assume an isotropic disruption, with the ejection velocity components Gaussian, with the dispersion proportional to $1/D$, and $V_5 = 93 \text{ m s}^{-1}$ for $D_5 = 5 \text{ km}$, an estimate based on our previous work (Vokrouhlický et al., 2006). Consequently, the distribution of the velocity magnitude $|\vec{v}_{ej}|$ is Maxwellian (see Figure 6). We start with 6 545 synthetic bodies, with the SFD covering $D \in (1.5; 100) \text{ km}$. Spins are also isotropic and periods uniform, $P \in (2; 10) \text{ h}$.

The thermal parameters remain the same as in our previous works: the bulk density $\rho = 2 500 \text{ kg m}^{-3}$, the surface density $\rho = 1 500 \text{ kg m}^{-3}$, the conductivity $K = 0.001 \text{ W m}^{-1} \text{ K}^{-1}$, the specific capacity $C = 680 \text{ J kg}^{-1}$, the Bond albedo $A = 0.1$, the infrared emissivity $\epsilon = 0.9$. **For simplicity, we assumed these parameters to be constants, although some of them may be**

size-dependent (as K in Delbo et al. 2015), or temperature-dependent (Anderson et al., 1991).

The free parameters of our model are the maximum of velocity distribution v_{max} (Fig. 6), the true anomaly f_{imp} , and the argument of pericentre ω_{imp} at the time of impact, which are interrelated by means of the Gauss equations. We may be forced to tune also other osculating orbital elements of the parent body, but for the moment we take those of (221) Eos as the nominal case.

Among the fixed parameters is the bulk density ρ . Usually, the age scales linearly with ρ due to the non-gravitational accelerations. Theoretically, if there are both gravitational and non-gravitational accelerations acting at the same time (e.g. Yarkovsky drift in a and chaotic diffusion in e) we may be able to break this degeneracy. However, based on our previous experience, we do not expect this for Eos. Neighbouring Veritas may be more suitable for this approach, by the way. Alternatively, one can use collisional models which exhibit a different scaling with ρ (cf. Sec. 4.1).

We integrate the equations of motion with the time step $\Delta t = 91 \text{ d}$, and the time span 4 Gyr. The output time step after computations of mean elements, proper elements, and final running-window filter is $\Delta t_{out} = 10 \text{ Myr}$.

2.5. Black-box method

We can eventually proceed with a so-called ‘black-box’ method (see Figure 7)¹: (i) we choose 180 boxes with $\Delta a = 0.0243 \text{ au}$, $\Delta e = 0.025$, $\Delta \sin I = 0.240$ in our case aligned with the J7/3 and J9/4 resonances²; (ii) count the numbers of observed asteroids located in these boxes; (iii) compute the observed incremental SFD globally, in the full domain; (iv) compute the background incremental SFD globally; (v) at every single output time step we compute the synthetic incremental SFD globally again (saving also lists of bodies in the respective size bins); (vi) for every single size bin ($D, D + dD$) we draw a synthetic background population of N_{bg} bodies from a random uniform distribution (in the whole range of $a_p, e_p, \sin I_p$); if the volume where the background was selected differs from our volume of interest, we have to use a suitable factor, i.e. fN_{bg} ; (vii) we *scale* the synthetic SFD to the observed one by randomly choosing $N_{obs} - fN_{bg}$ bodies from the lists above; (viii) we count the numbers of all synthetic asteroids located in the boxes; (ix) finally, we compute the metric

$$\chi^2 = \sum_{i=1}^{N_{box}} \frac{(N_{syn i} - N_{obs i})^2}{\sigma_{syn i}^2 + \sigma_{obs i}^2}, \quad (1)$$

where the uncertainties are assumed Poisson-like, $\sigma = \sqrt{N}$. Using both σ_{obs} and σ_{syn} in the denominator prevents ‘extreme’ χ^2 contributions in boxes where $N_{obs} \rightarrow 0$. We shall keep in mind **though** the corresponding probability distribution of χ^2 may be somewhat skewed. **There is some freedom related**

¹see <http://sirrah.troja.mff.cuni.cz/~mira/eos/eos.html> for an implementation in Python

²possibly also in D

211 **to the box sizes (binning), but within the limits of mean-**261
212 **ingfulness (neither a single box nor zillions of boxes), the**262
213 **method should give statistically comparable results as we**263
214 **always analyse the same information.**264

215 Unlike traditional simplified methods fitting an envelope to265
216 (a_p, H) or $(a_p, 1/D)$, we shall obtain not only an upper limit for
217 the age, but also a lower limit.266

218 3. Results

219 Hereinafter, we discuss not only the best-fit model, but also271
220 several bad fits which are actually more important, because the272
221 ‘badness-of-fit’ assures a solid conclusion about the Eos family.273

222 3.1. The nominal model

223 The nominal model is presented in Figure 7. We focus on the276
224 proper semimajor axis a_p vs proper eccentricity e_p distribution,277
225 having only one box in inclination $\sin I_p$. The initial conditions278
226 (top left) are so different from the observations (bottom middle)279
227 it is almost hopeless to expect a good fit anytime in the future.280
228 However, at around $t = 1.3$ Gyr the situation suddenly changes281
229 (top middle); it is almost unbelievable that the synthetic family282
230 is so similar to the observations! The final state (top right) is283
231 again totally different. The χ^2 reaches values as low as N_{box} ,284
232 so we may consider the best fit to be indeed reasonable. The285
233 age interval is $t = (1.3 \pm 0.3)$ Gyr. Let us emphasize that the286
234 fit so good only because we carefully accounted for all three287
235 problems outlined in Section 2.288

236 3.2. Bad fit 1: Ejection velocity tail

237 Because our sample is 3 times larger than the observed sam-291
238 ple, we can easily resample our synthetic bodies without actu-292
239 ally computing the N-body simulation anew, e.g. selecting only293
240 those with low ejection velocity $v_{\text{ej}} < 200 \text{ m s}^{-1}$. Consequently,
241 all bodies are initially located above the J7/3 resonance, and294
242 below the J11/5.

243 Using the same post-processing as above we arrived at Fig-295
244 ure 8. It is clear that the ‘best fit’ is actually a bad fit compared296
245 to the nominal model. The notable differences are below the297
246 J7/3 resonance, and above the J11/5 where the numbers of bod-298
247 ies are never sufficient to match the observations (cf. Fig. 7,299
248 bottom middle).300

249 It is worth to note there is a small family just below the J7/3301
250 resonance, namely (36256) 1999 XT₁₇ (FIN 629). Tsirvoulis302
251 et al. (2018) discovered a link to Eos by analysing the overall303
252 V-shape in the semimajor axis a_p vs the absolute magnitude H 304
253 diagram. It seems aligned with the original velocity field of305
254 the Eos family — it has the same $\sin I_p$ as the family core, but306
255 slightly larger $e_p \simeq 0.1$, because of the ‘ellipse’ in (a_p, e_p) vis-307
256 ible in Fig. 7 (top left). We thus conclude, (36256) family is308
257 actually a *remnant* of the original velocity field.309

258 If this is true, it may further contribute to the contamination310
259 of the ‘pristine zone’ between the J7/3 and J5/2 resonances,311
260 apart from low-probability crossings of the former resonance.312

This region was analysed by Tsirvoulis et al. (2018), where au-
thors carefully subtracted the contribution of all families (in-
cluding Eos), extracted the SFD of remaining background aster-
oids and computed the slope of the primordial (post-accretion)
SFD.

3.3. Bad fit 2: Parent body inclination

267 If we look on contrary on the proper semimajor axis a_p vs
268 proper inclination $\sin I_p$ distribution (Figure 9) there is a prob-
269 lem with the nominal model. Inclinations are all the time too
270 low (and the χ^2 too high compared to N_{box}). **This would affect**
271 **a 3-dimensional fit too, of course.**

272 Nevertheless, it seems sufficient to adjust the inclination by
273 approximately 0.005 rad to get a significantly better fit, χ^2 de-
274 creased from 238 down to 181. This seems still too high
275 wrt. 130, but this approach is possibly too simplified, because
276 we only shifted the output data. In reality, the resonances (in
277 particular the z_1) do not shift at all, they are determined by the
278 positions of giant planets, and we should perform the N-body
279 integration anew to obtain a correct $(a_p, \sin I_p)$ distribution.

3.4. Bad fit 3: True anomaly $f_{\text{imp}} < 120^\circ$

To demonstrate the sensitivity of our ‘black-box’ method
with respect to the impact parameters, we present an alterna-
tive N-body simulation which started with the true anomaly
 $f_{\text{imp}} = 0^\circ$. The orientation of the ellipse is then the opposite
and there is practically no chance for a good fit (see Figure 10).

All the time, there is a serious mismatch within the family
core, it is impossible explain the observed bodies in the boxes
with $a_p \simeq 2.97$ au, and $e_p \simeq 0.08$. Generally, it is surprising
that even 1.3 Gyr after the impact, there are clear traces of the
original velocity field! As already reported in Brož and Mor-
bidelli (2013), the ‘true’ true anomaly should be $f > 120^\circ$.
Another example of such traces (in inclination) is Koronis
family (Carruba et al., 2016).

4. Conclusions

Let us conclude, it is important to use a suitable selection of
asteroids, match the size-frequency distributions, and account
for the background population, when comparing N-body simu-
lations with observations. To this point, we presented and tested
a simple method how to compare a 3-dimensional distribution
of proper elements.

For the Eos family, it is possible to explain its shape in the
 $(a_p, e_p, \sin I_p)$ space and estimate the age at the same time, but
this estimate still scales with the bulk density ρ , because most of
the perturbations are non-gravitational (including all systematic
drifts $da/dt, de/dt, dI/dt$).

While we believe our model includes the key contributions,
no dynamical model is complete. For example, we miss inner
planets, gravitational perturbations by large asteroids, or short-
term spin axis evolution due to gravitational (solar) torques. Ini-
tial condition might be also too simple. In particular, the veloc-
ity field might have been non-isotropic even though in catas-
trophic disruptions (like Eos) we rather expect a high degree of

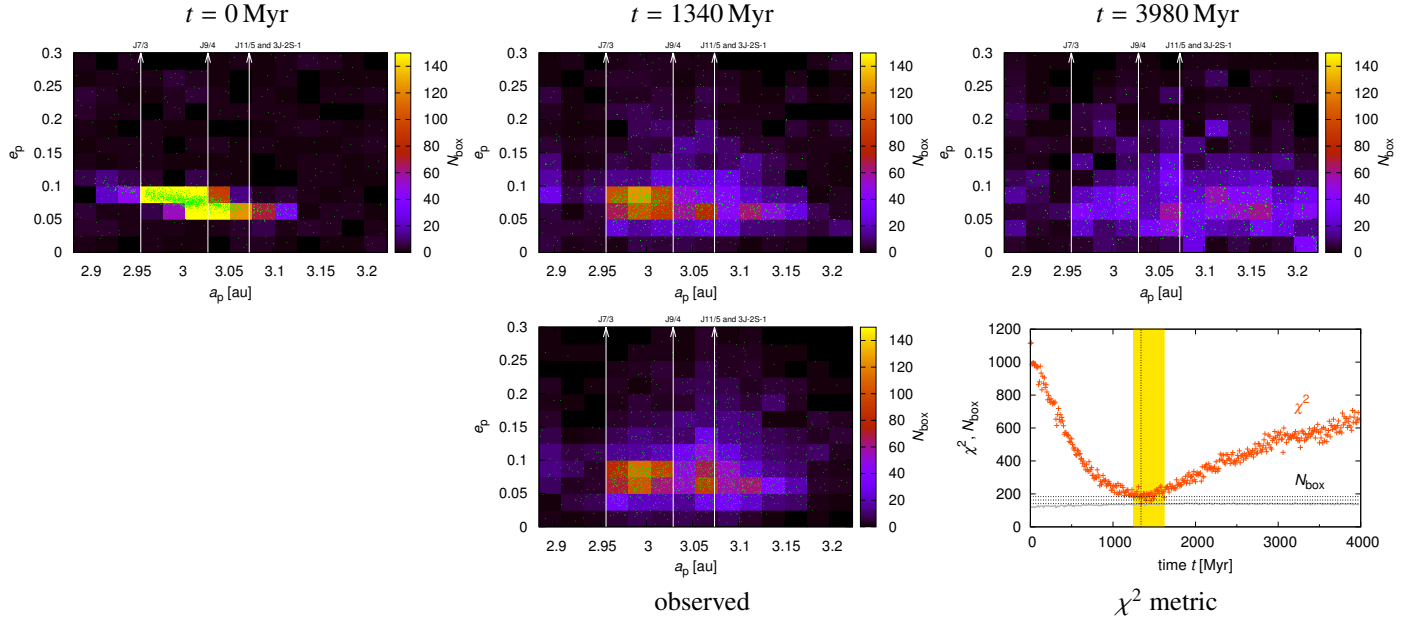


Figure 7: The proper semimajor axis a_p vs proper eccentricity e_p for the nominal simulation scaled to the observed SFD (as described in the main text) (top row). Bodies are plotted as green dots. Colours correspond to the number of bodies in 180 boxes, outlined by $\Delta a = 0.0234$ au, $\Delta e = 0.025$. The range of inclinations is always $\sin I_p \in (0.06; 0.30)$. Positions of major mean-motion and 3-body resonances are also indicated (J7/3, J9/4, J11/5, and 3J-2S-1). The z_1 secular resonance goes approximately from the lower-left corner to the upper-right. There are the initial conditions (left column), the best-fit at $t = 1340$ Myr (middle), the end of simulation (right); as well as the observations (bottom middle), and the respective χ^2 metric compared to the actual number of boxes N_{box} (bottom right). The correspondence between the best-fit and the observations is surprisingly good, with $\chi^2 = 141$, $N_{\text{box}} = 134$ (not all boxes are populated), and $\chi^2 \approx N_{\text{box}}$. The 1- σ , 2- σ and 3- σ levels (dotted lines) and the inferred 3- σ uncertainty of the age (yellow strip) are indicated too.

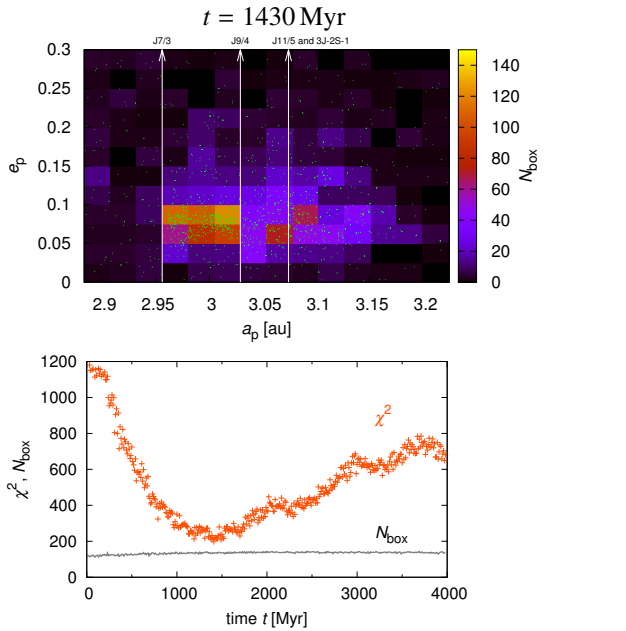


Figure 8: Bad fit 1: the proper semimajor axis a_p vs proper eccentricity e_p (top panel), and the temporal evolution of χ^2 (bottom panel) for a subset of bodies with the ejection velocities $v_{\text{ej}} < 200 \text{ m s}^{-1}$, i.e. without the tail of the distribution. Initially, all bodies were located above the J7/3 resonance. Observations were shown in Fig. 7 (bottom middle). The 'best-fit' at $t = 1430$ Myr, with $\chi^2 = 197$, $N_{\text{box}} = 134$, is much worse than the nominal case. The number of bodies below the J7/3 resonance is too low. Consequently, the velocity tail is needed to get a better fit.

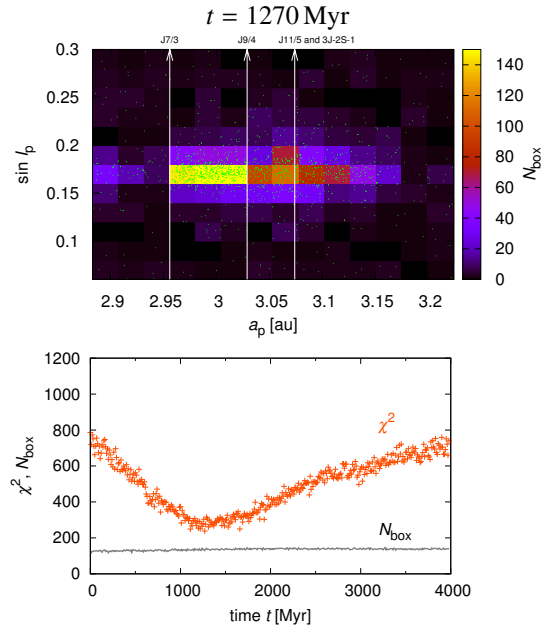


Figure 9: Bad fit 2: the proper semimajor axis a_p vs proper inclination $\sin I_p$ for the synthetic population (top panel), and the temporal evolution of χ^2 (bottom panel). The boxes are consequently different, $\Delta a = 0.0243$ au, $\Delta \sin I = 0.02$, $e_p \in (0.0; 0.3)$, so is the resulting 'best-fit' value $\chi^2 = 238$, $N_{\text{box}} = 130$. The parent body would have to be shifted in inclination by approximately 0.005 rad to get a better fit.

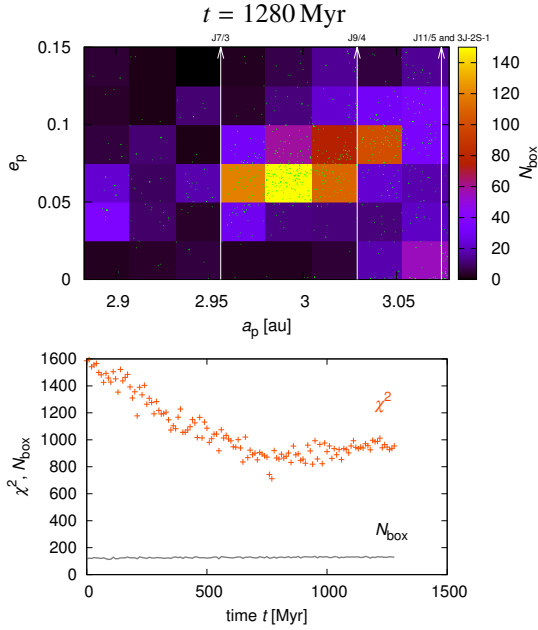


Figure 10: Bad fit 3: a detail of the proper semimajor axis a_p vs proper eccentricity e_p (top panel), and the temporal evolution of χ^2 (bottom panel) for the simulation with the true anomaly at the time of impact $f_{\text{imp}} = 0^\circ$, and the argument of perihelion $\omega_{\text{imp}} = 30^\circ$. The ‘best-fit’ $\chi^2 = 711$ is so high compared to $N_{\text{box}} = 124$ that the simulation was not computed up to 4000 Myr. The value has to be $f \gtrsim 120^\circ$ to get a better fit.

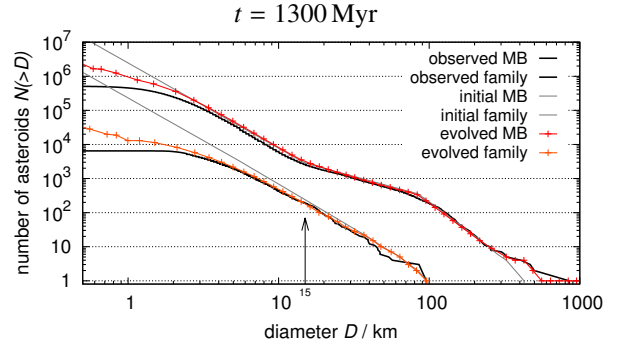


Figure 11: The cumulative size-frequency distributions computed by our Monte-Carlo collisional model of the two populations: the main belt (red), the Eos family (orange), together with the respective initial conditions (gray), and observations (black). At the time around $t = 1300$ Myr the correspondence is good, except the tail below $D \lesssim 2$ km where an observational incompleteness makes the SFD’s shallow. In particular, we successfully fit the knee of the family at $D \approx 15$ km.

isotropy (Ševeček et al., 2017). Generally, it is better to keep both as simple as possible to have the lowest possible number of free parameters.

Let us finally compare our nominal best-fit model to another two distributions (size and spin) and the respective models (collisional and rotational).

4.1. Collisional evolution

In a Monte-Carlo collisional model, size-frequency distributions are evolved due to fragmentation and reaccumulation. We assume two populations: the main belt, and the Eos family. Their physical properties are summarized by the scaling law $Q_D^*(r)$, for which we assume parameters of basalt from Benz and Asphaug (1999). To compute the actual evolution, we use the Boulder code by Morbidelli et al. (2009). Parametric relations in the Boulder code, which are needed to compute the fragment distributions, are derived from SPH simulations of Durda et al. (2007).

We assume the initial SFD of the main belt relatively similar to the currently observed SFD, because we focus on the already stable solar system, with the fixed intrinsic impact probability $P_{\text{imp}} = 3.1 \times 10^{-18} \text{ km}^{-2} \text{ yr}^{-1}$ and the mean velocity $v_{\text{imp}} = 5.28 \text{ km s}^{-1}$. The initial SFD of the Eos family has the same slope as the observed SFD in the range $D \in (15; 50) \text{ km}$, and it is prolonged down to $D_{\text{min}} = 0.005 \text{ km}$. We also account for the size-dependent dynamical decay due to the Yarkovsky effect, with $N(t + \Delta t) = N(t) \exp(-\Delta t / \tau)$, where the time scale $\tau(D)$ is taken from Bottke et al. (2005).

The resulting collisional evolution is shown in Figure 11. The observed knee at $D \approx 15 \text{ km}$ is very important, because

it usually arises from a collisional grinding. If we start with the constant slope from above, we can match the observed SFD at about 1.3 Gyr which is in accord with the dynamics.

It is worth to note the scaling of the age with the bulk density ρ is different from dynamics, which in principle allows to resolve the problem. However, the collisional model is sensitive to the initial conditions and using a steeper SFD would result in longer age. In other words, everything is based on the simple assumption of the constant slope. It would be useful to base the initial conditions on a specific SPH model for the Eos family, with the parent body size reaching up to 380 km (according to an extrapolation of Durda et al. 2007 results).

4.2. Spin distribution

At the same time, it is worth to check the observed distribution of pole latitudes β , reported in Hanuš et al. (2018). Our dynamical model evolves the spin (ω, γ) , which affects the Yarkovsky drift rate da/dt , but we do not account for spin-orbital resonances (so we would not explain a clustering in the Koronis family; Slivan 2002). Nevertheless, if we use the current model for Eos, with the same post-processing, but focus on $(a_p, \sin \beta)$ boxes instead, we obtain the results summarized in Figure 12.

We start from an isotropic distribution of spins, which means isotropic also in $\sin \beta$. After about 1.3 Gyr, it is possible to fit both the asymmetry of the distribution with respect to $a_c = 3.014 \text{ au}$, and the substantially lower number of bodies at mid-latitudes $|\sin \beta| < 0.5$. There are two systematics still present in our analysis, as we account neither for the observational selection bias, nor for the bias of the inversion method, but they should not overturn our conclusions.

Unfortunately, the uncertainty is larger than in the nominal model, because the number of bodies with known latitudes is limited, namely 46 within the family core. As a solution, we may use the distribution of $|\beta|$ of Cibulková et al. (2016) which is available for many more asteroids, but we would need to determine the ‘point-spread function’, describing a relation between input $|\beta|$ and output $|\beta|$ for this (approximate) method,

379 which smears the distribution substantially. Their sample also
 380 contains a lot of bodies smaller than we had in the previous sim-
 381 ulations, so we would have to compute everything again. This
 382 is postponed as a future work.

383 Acknowledgements

384 The work of MB has been supported by the Grant Agency
 385 of the Czech Republic (grant no. P209-18-04514J). In this pa-
 386 per, we used observations made by BlueEye 600 robotic ob-
 387 servatory, supported by the Technology Agency of the Czech
 388 Republic (grant no. TA03011171). **We thank V. Carruba and**
 389 **an anymous referee (F. R.) for their valuable input.**

390 References

391 Anderson, O.L., Isaak, D.L., Oda, H., 1991. Thermoelastic parameters for six
 392 minerals at high temperature. *J. Geophys. Res.* 96, 18037. doi:10.1029/
 393 91JB01579.

394 Benz, W., Asphaug, E., 1999. Catastrophic Disruptions Revis-
 395 ited. *Icarus* 142, 5–20. doi:10.1006/icar.1999.6204,
 396 arXiv:arXiv:astro-ph/9907117.

397 Bottke, W.F., Durda, D.D., Nesvorný, D., Jedicke, R., Morbidelli, A., Vokrouh-
 398 lický, D., Levison, H.F., 2005. Linking the collisional history of the main
 399 asteroid belt to its dynamical excitation and depletion. *Icarus* 179, 63–94.
 400 doi:10.1016/j.icarus.2005.05.017.

401 Brož, M., Morbidelli, A., 2013. The Eos family halo. *Icarus* 223, 844–849.
 402 doi:10.1016/j.icarus.2013.02.002, arXiv:1302.1447.

403 Brož, M., Vokrouhlický, D., Morbidelli, A., Nesvorný, D., Bottke, W.F., 2011.
 404 Did the Hilda collisional family form during the late heavy bombardment?
 405 *Mon. Not. R. Astron. Soc.* 414, 2716–2727. doi:10.1111/j.1365-2966.
 406 2011.18587.x, arXiv:1109.1114.

407 Čapek, D., Vokrouhlický, D., 2004. The YORP effect with finite thermal con-
 408 ductivity. *Icarus* 172, 526–536. doi:10.1016/j.icarus.2004.07.003.

409 Carruba, V., Domingos, R.C., Nesvorný, D., Roig, F., Huaman, M.E., Souami,
 410 D., 2013. A multidomain approach to asteroid families' identification.
 411 *Mon. Not. R. Astron. Soc.* 433, 2075–2096. doi:10.1093/mnras/stt884,
 412 arXiv:1305.4847.

413 Carruba, V., Nesvorný, D., Aljbaae, S., 2016. Characterizing the origi-
 414 nal ejection velocity field of the Koronis family. *Icarus* 271, 57–66.
 415 doi:10.1016/j.icarus.2016.01.006, arXiv:1602.04491.

416 Carruba, V., Nesvorný, D., Aljbaae, S., Huaman, M.E., 2015. Dynamical evo-
 417 lution of the Cybele asteroids. *Mon. Not. R. Astron. Soc.* 451, 244–256.
 418 doi:10.1093/mnras/stv997, arXiv:1505.03745.

419 Cibulková, H., Ďurech, J., Vokrouhlický, D., Kaasalainen, M., Oszkiewicz,
 420 D.A., 2016. Distribution of spin-axes longitudes and shape elongations
 421 of main-belt asteroids. *Astron. Astrophys.* 596, A57. doi:10.1051/
 422 0004-6361/201629192, arXiv:1610.02790.

423 Delbo, M., Mueller, M., Emery, J.P., Rozitis, B., Capria, M.T., 2015. Asteroid
 424 Thermophysical Modeling. pp. 107–128.

425 Durda, D.D., Bottke, W.F., Nesvorný, D., Enke, B.L., Merline, W.J., Asphaug,
 426 E., Richardson, D.C., 2007. Size-frequency distributions of fragments from
 427 SPH/ N-body simulations of asteroid impacts: Comparison with observed
 428 asteroid families. *Icarus* 186, 498–516. doi:10.1016/j.icarus.2006.
 429 09.013.

430 Farinella, P., Vokrouhlický, D., Hartmann, W.K., 1998. Meteorite Delivery via
 431 Yarkovsky Orbital Drift. *Icarus* 132, 378–387. doi:10.1006/icar.1997.
 432 5872.

433 Hanuš, J., Delbo', M., Alí-Lagoa, V., Bolin, B., Jedicke, R., Ďurech, J.,
 434 Cibulková, H., Pravec, P., Kušnirák, P., Behrend, R., Marchis, F., Antonini,
 435 P., Arnold, L., Audejean, M., Bachschmidt, M., Bernasconi, L., Brunetto, L.,
 436 Casulli, S., Dymock, R., Esseiva, N., Esteban, M., Gerteis, O., de Groot, H.,
 437 Gully, H., Hamanowa, H., Hamanowa, H., Krafft, P., Lehký, M., Manzini,
 438 F., Michelet, J., Morelle, E., Oey, J., Pilcher, F., Reigier, F., Roy, R., Sa-
 439 lom, P.A., Warner, B.D., 2018. Spin states of asteroids in the Eos colli-
 440 sional family. *Icarus* 299, 84–96. doi:10.1016/j.icarus.2017.07.007,
 441 arXiv:1707.05507.

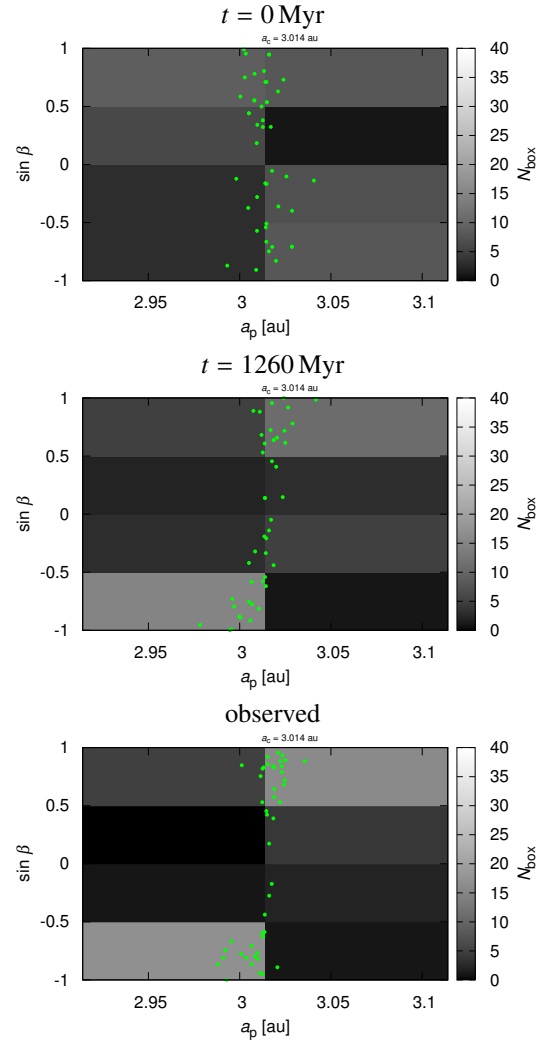


Figure 12: The proper semimajor axis a_p vs the sine of pole latitude $\sin\beta$ **for the initial synthetic population (top panel), the evolved synthetic population (middle), and the observed population of 46 bodies (bottom).** The individual bodies are shown as green dots, while their numbers in 8 boxes are indicated by the gray scale. The simulation started from initially isotropic **random** distribution, i.e. isotropic in $\sin\beta$. The synthetic SFD was again scaled to the observed one. We account neither for the observational selection bias, nor for the bias of the inversion method. Nevertheless, it is possible to fit both the asymmetry of the distribution with respect to $a_c = 3.014$ au, and the substantially lower number of bodies at mid-latitudes $|\sin\beta| < 0.5$.

442 Hanuš, J., Ďurech, J., Brož, M., Warner, B.D., Pilcher, F., Stephens, R., Oey, J.,
443 Bernasconi, L., Casulli, S., Behrend, R., Polishook, D., Hensch, T., Lehký,
444 M., Yoshida, F., Ito, T., 2011. A study of asteroid pole-latitude distribution
445 based on an extended set of shape models derived by the lightcurve inver-
446 sion method. *Astron. Astrophys.* 530, A134. doi:10.1051/0004-6361/
447 201116738, arXiv:1104.4114.

448 Hirayama, K., 1918. Groups of asteroids probably of common origin. *Astron.*
449 *J.* 31, 185–188. doi:10.1086/104299.

450 Knežević, Z., Milani, A., 2003. Proper element catalogs and asteroid fam-
451 ilies. *Astron. Astrophys.* 403, 1165–1173. doi:10.1051/0004-6361:
452 20030475.

453 Laskar, J., Robutel, P., 2001. High order symplectic integrators for perturbed
454 Hamiltonian systems. *Celestial Mechanics and Dynamical Astronomy* 80,
455 39–62. arXiv:arXiv:astro-ph/0005074.

456 Levison, H.F., Duncan, M.J., 1994. The long-term dynamical behavior of short-
457 period comets. *Icarus* 108, 18–36. doi:10.1006/icar.1994.1039.

458 Masiero, J.R., Mainzer, A.K., Grav, T., Bauer, J.M., Cutri, R.M., Dai-
459 ley, J., Eisenhardt, P.R.M., McMillan, R.S., Spahr, T.B., Skrutskie, M.F.,
460 Tholen, D., Walker, R.G., Wright, E.L., DeBaun, E., Elsbury, D., Gau-
461 tier, IV, T., Gomillion, S., Wilkins, A., 2011. Main Belt Asteroids with
462 WISE/NEOWISE. I. Preliminary Albedos and Diameters. *Astrophys. J.*
463 741, 68. doi:10.1088/0004-637X/741/2/68, arXiv:1109.4096.

464 Morbidelli, A., Bottke, W.F., Nesvorný, D., Levison, H.F., 2009. Asteroids
465 were born big. *Icarus* 204, 558–573. doi:10.1016/j.icarus.2009.07.
466 011, arXiv:0907.2512.

467 Mothé-Diniz, T., Carvano, J.M., Bus, S.J., Duffard, R., Burbine, T.H., 2008.
468 Mineralogical analysis of the Eos family from near-infrared spectra. *Icarus*
469 195, 277–294. doi:10.1016/j.icarus.2007.12.005.

470 Nesvorný, D., Brož, M., Carruba, V., 2015. Identification and Dynamical Prop-
471 erties of Asteroid Families. pp. 297–321.

472 Novaković, B., Tsirvoulis, G., 2014. Recent disruption of an asteroid from
473 the Eos family, in: Muinonen, K., Penttilä, A., Granvik, M., Virkki, A.,
474 Fedorets, G., Wilkman, O., Kohout, T. (Eds.), *Asteroids, Comets, Meteors*
475 2014.

476 Parker, A., Ivezić, Ž., Jurić, M., Lupton, R., Sekora, M.D., Kowalski, A., 2008.
477 The size distributions of asteroid families in the SDSS Moving Object Cat-
478 alog 4. *Icarus* 198, 138–155. doi:10.1016/j.icarus.2008.07.002,
479 arXiv:0807.3762.

480 Pravec, P., Harris, A.W., 2000. Fast and Slow Rotation of Asteroids. *Icarus*
481 148, 12–20. doi:10.1006/icar.2000.6482.

482 Quinn, T.R., Tremaine, S., Duncan, M., 1991. A three million year integration
483 of the earth’s orbit. *Astron. J.* 101, 2287–2305. doi:10.1086/115850.

484 Ševeček, P., Brož, M., Nesvorný, D., Enke, B., Durda, D., Walsh, K., Richard-
485 son, D.C., 2017. SPH/N-Body simulations of small ($D = 10$ km) asteroidal
486 breakups and improved parametric relations for Monte-Carlo collisional
487 models. *Icarus* 296, 239–256. doi:10.1016/j.icarus.2017.06.021.

488 Šidlichovský, M., Nesvorný, D., 1996. Frequency modified Fourier transform
489 and its applications to asteroids. *Celestial Mechanics and Dynamical As-
490 tronomy* 65, 137–148. doi:10.1007/BF00048443.

491 Slivan, S.M., 2002. Spin vector alignment of Koronis family asteroids. *Nature*
492 419, 49–51. doi:10.1038/nature00993.

493 Tsirvoulis, G., Morbidelli, A., Delbo’, M., Tsiganis, K., 2018. Reconstructing
494 the size distribution of the primordial Main Belt. *Icarus* 304, 14–23.

495 Vokrouhlický, D., 1998. Diurnal Yarkovsky effect as a source of mobility of
496 meter-sized asteroidal fragments. I. Linear theory. *Astron. Astrophys.* 335,
497 1093–1100.

498 Vokrouhlický, D., Brož, M., Morbidelli, A., Bottke, W.F., Nesvorný, D., Laz-
499 zaro, D., Rivkin, A.S., 2006. Yarkovsky footprints in the Eos family. *Icarus*
500 182, 92–117. doi:10.1016/j.icarus.2005.12.011.

501 Vokrouhlický, D., Farinella, P., 1999. The Yarkovsky Seasonal Effect on Aster-
502 oidal Fragments: A Nonlinearized Theory for Spherical Bodies. *Astron. J.*
503 118, 3049–3060. doi:10.1086/301138.

504 Zappalà, V., Bendjoya, P., Cellino, A., Farinella, P., Froeschlé, C., 1995. Aster-
505 oid families: Search of a 12,487-asteroid sample using two different cluster-
506 ing techniques. *Icarus* 116, 291–314. doi:10.1006/icar.1995.1127.